DYNA
http://dyna.medellin.unal.edu.co/

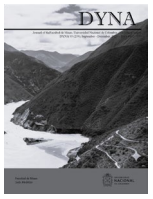

UNIVERSIDAD NACIONAL DE COLOMBIA

Impact of printing strategies and thermal debinding atmosphere on the microstructure and mechanical properties of M2 tool steel produced via fused filament fabrication

Theylor Andres Amaya-Villabon [a], Andres Fernando Gil-Plazas [b], Julián David Rubiano-Buitrago [a] & Liz Karen Herrera-Quintero [a]

[a] *Universidad Nacional de Colombia – Sede Bogotá, Facultad de Ingeniería, Departamento de Ingeniería Mecánica y Mecatrónica, Grupo de Investigación AFIS, Laboratorio de Fundición y Pulvimetalurgia, Bogotá, Colombia. taamayav@unal.edu.co, judrubianobu@unal.edu.co, lkherreraq@unal.edu.co*

[b] *SENA, Centro de Materiales y Ensayos - Regional Distrito Capital, Grupo de Investigación GIMES, Bogotá, Colombia. agilp@sena.edu.co*

Received: August 14th, 2024. Received in revised form: November 13th, 2024. Accepted: December 2nd, 2024.

Abstract
This research investigates the effects of printing strategies and thermal debinding atmosphere on the microstructure and mechanical properties of M2 tool steel samples obtained by Fused Filament Fabrication. A comparative analysis was conducted between concentric and linear printing patterns. Printed samples were subjected to different thermal debinding heating rates in nitrogen and vacuum atmospheres to evaluate their effects on mechanical properties, such as microhardness and Transverse Rupture Strength (TRS). The assessment of the results showed a consistent correlation between microstructure and mechanical properties, confirmed by metallography and ANOVA statistical test studies. The study concluded that a nitrogen atmosphere enhances densification and strength by retaining higher carbon content, whereas a vacuum atmosphere leads to increased porosity and reduced strength. Finally, these findings offer valuable insights for optimizing sintering processes to improve material properties.

Keywords: thermal debinding; additive manufacturing; M2 steel.

Impacto de las estrategias de impresión y de la atmósfera de despolimerización térmica en la microestructura y las propiedades mecánicas del acero de herramientas M2 producido mediante fabricación por fusión de filamentos

Resumen
Esta investigación indaga el efecto de la estrategia de impresión y de la atmósfera de despolimerizado térmico en la microestructura y las propiedades mecánicas de muestras de acero M2 obtenido mediante fabricación con filamento fundido. Se realizó un análisis comparativo entre patrones de impresión concéntricos y lineales. Las muestras impresas se sometieron a diferentes velocidades de despolimerizado térmico en atmósferas de nitrógeno y vacío para evaluar sus efectos sobre las propiedades mecánicas, como la microdureza y la resistencia a la ruptura transversal (TRS). La evaluación de los resultados mostró una correlación continua entre la microestructura y las propiedades mecánicas, confirmada mediante metalografía y pruebas estadísticas ANOVA. El estudio concluyó que una atmósfera de nitrógeno mejora la densificación y la resistencia mecánica al retener un mayor contenido de carbono; mientras que una atmósfera de vacío aumenta la porosidad y reduce la resistencia. Estos hallazgos ofrecen información valiosa para optimizar los procesos de sinterización para mejorar las propiedades de los materiales.

Palabras clave: despolimerizado térmico; manufactura aditiva; acero M2.

How to cite: Amaya-Villabon, T.A., Gil-Plazas, A.F., Rubiano-Buitrago, J.D., and Herrera-Quintero, K., Impact of printing strategies and thermal debinding atmosphere on the microstructure and mechanical properties of M2 tool steel produced via fused filament fabrication, DYNA, (92)239, pp. 9-18, October - December, 2025.

1 Introduction

Nowadays, additive manufacturing has become a widely studied process with significant advancements over the last decade [1]. Additive manufacturing in metals has had a great impact on the industry, leading to the development of various techniques such as Directed Energy Deposition (DED) [2], Wire Arc Additive Manufacturing (WAAM) [3], Laser Metal Deposition (LMD) [4], Electron Beam Additive Manufacturing (EBAM) [5] and Laser-Powder-based DED (LP-DED) [6]. These techniques offer significant advantages, including high-speed deposition rates. However, the layer-by-layer approach creates a molten pool, which can lead to anisotropic behavior in the final product. Despite this, heat treatment can homogenize the microstructure and mitigate these effects [7-9].

Now being applied to metals, Fused Filament Fabrication (FFF) technology is a variant of the Shaping-Debind-Sintering (SDS) processes, which has been used in Powder Injection Molding (PIM) for over five decades [10]. This approach is significantly more cost-effective than Directed Energy Deposition (DED) techniques. As a result, many research efforts focus on FFF for shaping due to its lower costs and practical applications.

PIM feedstocks are available in the form of pellets with a powder material content of about 55 Vol% to 65 Vol%, whereas FFF feedstocks are in the form of filaments with a powder material content of about 45 Vol% to 55 Vol% [11], [12]. The main difference lies in the fact that pellets require a vehicle solely for transportation, which is provided by polyolefins, waxes, and surfactants. In the case of filaments, the powder content is lower because the polymers acting as the vehicle tend to exhibit brittle behavior in filament form. To mitigate this issue, part of the powder is replaced with a thermoplastic elastomer to enhance elasticity [12].

Like PIM, FFF can process a wide range of materials including oxides [13] [14], metals [15], [16], and composites [17], among others. FFF offers an advantage in producing parts with minimal or reduced anisotropic behavior compared to the DED process. However, it is important to note that FFF exhibits relatively slow deposition rates. The quality of the printed parts can be compared to techniques such as Powder Bed Fusion (PBF) and Binder Jetting (BJ) [1].

In FFF, the filament is fed through a mechanism that transports the material into a heated zone where it melts. The molten material is then applied layer by layer to complete the desired geometry. The geometry is first modeled and then sliced to calculate the machine's movements (strategies). The mechanical strength of parts produced by FFF is influenced by these strategies, as the bonding between layers is crucial to the overall strength of the part [18].

M2 tool steel, also known as high-speed steel, derives its name from its ability to machine materials at high speeds. It is an alloy of steel that includes elements, which promote the alpha phase of iron, such as tungsten, molybdenum, and vanadium. M2 is characterized by high hardness and excellent abrasion resistance [19]. These properties make it commonly used in the manufacture of cutting tools and punching tools. Its microstructure provides high resistance to deformation and fatigue, making it particularly suitable for maintaining sharp edges in precise geometries. Therefore, ensures high tool durability.

One of the main advantages of using M2 tool steel in the fabrication of parts via the FFF process is its ability to reproduce complex geometries and designs for specific applications [20]. This includes specialized tools or components that require high hardness and excellent abrasion resistance properties that may be difficult to obtain through conventional manufacturing processes due to the complexity of their form and function.

The aim of this study is to provide insights into the behavior of printed parts produced via FFF, focusing on strategies to produce dense parts suitable for wear applications. It analyzes how different thermal debinding rates influence densification and mechanical properties. The findings of this research serve as a valuable resource for the tool manufacturing industry, including applications such as punching and other specialized tooling.

2 Materials and Methods

2.1 Raw materials

The M2 tool steel powders used in this study (Fig. 1) are nitrogen-atomized powders supplied by Chengdu Huarui Industrial CO., LTD. These powders possess a particle size ranging from 17 μm to 50 μm, with a chemical composition listed in Table 1. The powders were mixed with two polymers: a polyolefin-based backbone comprising polypropylene random-copolymer (PP) (Essentia, Cartagena, Colombia) and polypropylene grafted with maleic anhydride (PPMA), as well as a thermoplastic elastomer (TPE) (Sungallon, Shenzhen, China). The combination of these materials serves as feedstock to create a composite filament for the FFF process [16-17,21-27].

The feedstock was mixed using a shear-based machine to achieve the composition of 50 vol.% powders and 50 vol.% binder. This specific ratio was selected after testing several powder-to-binder mixtures, including 60/40 and 55/45. It was noticed that higher powder contents (e.g., 60 vol.% and 55 vol.%) increased the fragility of the filament, leading to breakage during handling and the FFF process. The 50/50 composition provided an optimal balance between powder

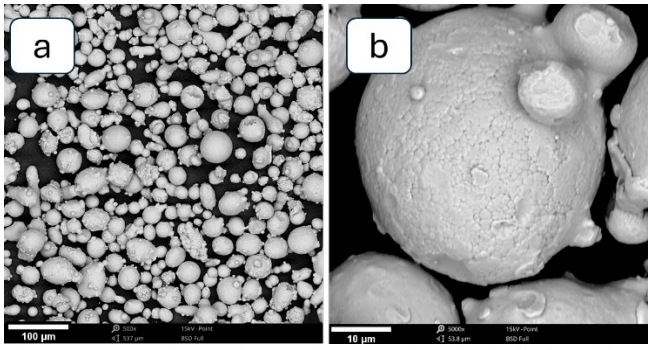

Figure 1. (a) SEM image of M2 tool steel powders, (b) detail of particles in M2 tool steel.
Source: Authors.

Table 1.
Chemical composition of M2 tool steel.

Element	Weight %
C	0.819
Si	0.43
Cr	3.99
W	5.68
Mo	4.56
V	1.76
Mn	0.27
S	0.007
P	0.013

Source: CHENGDU HUARUI INDUSTRIAL CO., LTD.

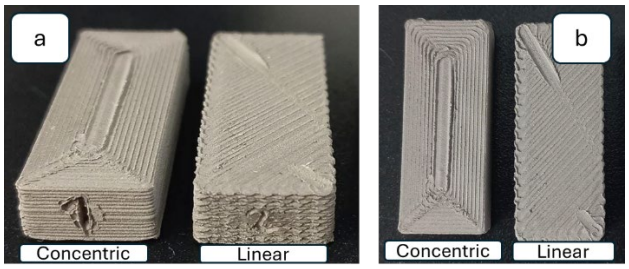

Figure 2. Concentric and linear printed samples, (a) Front view of green TRS samples(b) Top view of green TRS samples.
Source: Authors.

Table 2.
Printing parameters.

Parameter	Concentric pattern	Linear pattern
Printing flow	102 %	102 %
Infill overlap	50 %	50 %
Retraction	None	None
Nozzle temperature	225 °C	225 °C
Cooling fan	Off	Off
Printing speed	7.5 mm/s	7.5 mm/s

Source: Authors.

loading and filament flexibility, ensuring successful filament fabrication and printing. Finally, the selected binder composition for this study consisted of 60 wt.% of TPE and 40 wt.% of backbone (PP and PPMA).

After mixing, the material was cut into squares smaller than 5 mm. The filaments were produced using a single-screw extruder at temperatures ranging from 150°C to 180°C and spooled to obtain a diameter of 1.75 ± 0.08 mm. The final filament was found to have a real density of 4.73 g/cm³ and a linear density of 11.38 g/m. These properties are crucial for maintaining a steady and reliable material feed throughout the Fused Filament Fabrication (FFF) process.

2.2 Printing

Two different patterns were studied in this work: a linear pattern and a concentric pattern, the printing parameters are shown in Table 2. Sixteen TRS (Transverse Rupture Strength) samples were printed using an Ender 3 V2 FFF printer for each pattern, following the geometry specified in ASTM standard B528. Fig. 2 illustrates the obtained samples.

2.3 Debinding and sintering

The printed samples were subjected to solvent debinding using cyclohexane for 72 hours at 60 °C and 250 rpm. This step is crucial to dissolve the TPE, thereby promoting a porous network that helps in the removal of gases produced during thermal debinding.

Thermal debinding was examined by varying the heating rate: 0.5 °C/min, 1 °C/min, and 2 °C/min. In each case, the material was heated up to 200 °C with a plateau of 60 minutes, then heated up to 350 °C with a plateau of 120 minutes, and finally to 600 °C with a plateau of 60 minutes. These temperatures were selected based on TGA results, which showed plateaus corresponding to polymer pyrolysis. For each heating rate, two debinding atmospheres were selected vacuum at 10 Pa and nitrogen (N2) atmospheric pressure.

After thermal debinding, sintering was conducted by switching the atmosphere to an active gas mixture, specifically H_2N_2 (75 vol% H_2 – 25 vol% N_2), at a temperature of 1350 °C. At this temperature, Super Solidus Liquid Phase Sintering occurs, where the sintering temperature is above the alloy's solidus but below its liquidus point. This results in a small fraction of the material melting and forming a liquid phase while the majority remains solid. The presence of this liquid phase promotes better densification by enhancing particle rearrangement and atomic diffusion [28–30].

2.4 Characterization

The thermal degradation temperatures of the polymers were studied using thermogravimetric analysis (TGA) with a Mettler Toledo TGA 1 STARe System. The analysis was conducted in a nitrogen (N_2) atmosphere with a heating rate of 10 °C/min, ranging from 25 °C to 1000 °C. This procedure was performed in accordance with ASTM E1131-08, which outlines the standard test method for compositional analysis by thermogravimetry.

The density of the printed and sintered samples was determined using the Archimedes method, following ASTM B962-17, the standard test method for the density of compacted or sintered powder metallurgy (PM) products using Archimedes' principle. A Sartorius analytical balance equipped with a density determination kit was employed to measure the mass of the samples in air and submerged in distilled water at room temperature. The densities were calculated considering the buoyancy effect of water and correcting for air bubbles adhering to the sample surfaces.

For the metallographic analysis, samples were prepared following ASTM E3-11, 'Standard Guide for Preparation of Metallographic Specimens.' The sintered samples were sectioned using a metallographic cutter to obtain cross-sectional specimens without inducing significant mechanical deformation and then mounted in thermosetting epoxy resin for ease of handling during grinding and polishing. The mounted samples were sequentially ground with silicon carbide (SiC) abrasive papers of grit sizes 240, 400, 600, 800, and 1200 under water lubrication to prevent heat generation and microstructural alteration. Following grinding, the samples were polished using diamond suspensions of 6 µm, 3 µm, and 1 µm particle sizes on a polishing cloth to achieve a mirror-like surface finish. All polishing steps were

performed using a rotating polishing wheel at controlled speeds and pressures, adhering to ASTM E3-11 guidelines.

To reveal the microstructure, the polished samples were chemically etched with a 2 % Nital solution (2 ml nitric acid in 98 ml ethanol) for 10–15 seconds. This etchant selectively attacks the grain boundaries and carbide phases in M2 tool steel, enhancing the contrast between different microstructural features under microscopic examination.

Microstructural observations were performed using optical microscopy (Zeiss Axio Observer Z1.m) to assess the general microstructure, grain size, phase distribution, and porosity. High-resolution imaging was conducted using scanning electron microscopy (SEM) (Phenom XL), coupled with Energy-Dispersive X-ray Spectroscopy (EDS) for elemental analysis and phase identification.

Mechanical properties were evaluated through microhardness testing and transverse rupture strength (TRS) testing. Microhardness measurements were conducted using a Vickers microhardness tester according to ASTM E384-17, 'Standard Test Method for Microindentation Hardness of Materials.' A load of 500 gf was applied with a dwell time of 10 seconds, and several indentations were performed at both the edge and center of the sintered samples to assess hardness homogeneity. TRS tests were made on sintered specimens using a Shimadzu UH-50A universal testing machine at a crosshead speed of 1 mm/min, following ASTM B528, 'Standard Test Method for Transverse Rupture Strength of Powder Metallurgy (PM) Specimens.' Tests were performed at room temperature to determine the transverse rupture strength and deformation behavior of the material.

3 Results Analysis and Discussion

3.1 Green density

Initially, the study analyzed the influence of fill patterns on the green density of M2 tool steel specimens produced via Fused Filament Fabrication (FFF). As shown in the boxplot (Fig. 3), the green density of the samples varied depending on whether concentric or linear fill patterns were used. Notably, the linear fill pattern showed a higher median green density compared to the concentric fill pattern.

A closer examination of the nature of the fill patterns reveals that the linear pattern likely provides more consistent layer overlap, which may result in fewer gaps and a more uniform density throughout the sample.

In contrast, the concentric pattern, which follows the part's contour in concentric circles or ellipses, creates variable overlaps between layers. These variations can introduce inconsistencies in packing density, potentially causing differential shrinkage during the debinding and sintering processes.

To evaluate the differences observed in Fig. 3 a statistical analysis was made outlined in Table 3. According to the ANOVA results, the fill pattern has a statistically significant impact on the green density (p-value = 0.000068).

The statistical variability is attributed to the accumulation of defects produced by the printing strategy. The concentric pattern shows a higher presence of defects compared to the linear pattern, some observed

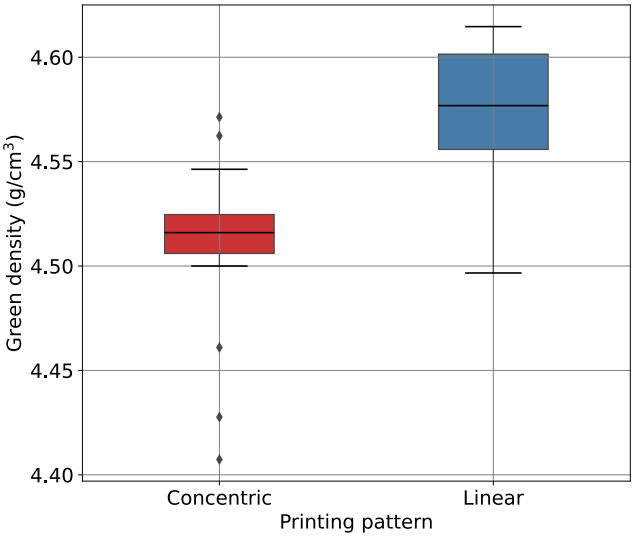

Figure 3. Green density of printed samples.
Source: Authors.

Table 3.
Results of the one-way ANOVA of green density.

Source	Sum_sq	Df	F	P-value
Pattern	0.033800	1.0	21.332498	0.000068
Residual	0.47533	30		

Source: Authors

concentric samples have a presence of porosity in area of 2.7 % compared to the linear pattern with a porosity of 1.9 %. Fig. 4 illustrates the transverse rupture of the samples in the green state, showing voids resulting from a lack of material between fill lines. This lack of material could be a consequence of insufficient printing flow; however, if the flow exceeds the amount, could lead to other defects such as “mountain-type” [17]. Nevertheless, the observed defects could be associated with variability in the filament diameter which is assumed to be randomly distributed all over the extruded filament. The resultant green density also reflects the capacity of each infill strategy to avoid this random effect.

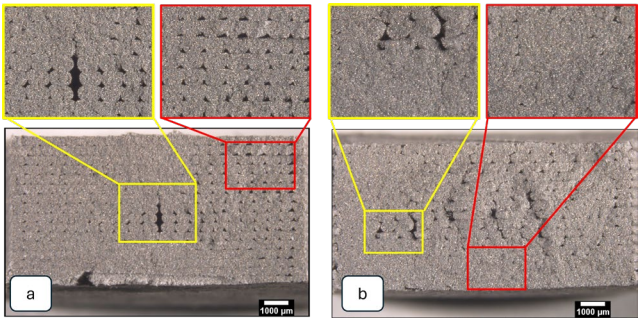

Figure 4. Transverse fracture of green samples, (a) Concentric pattern, (b) linear pattern.
Source: Authors.

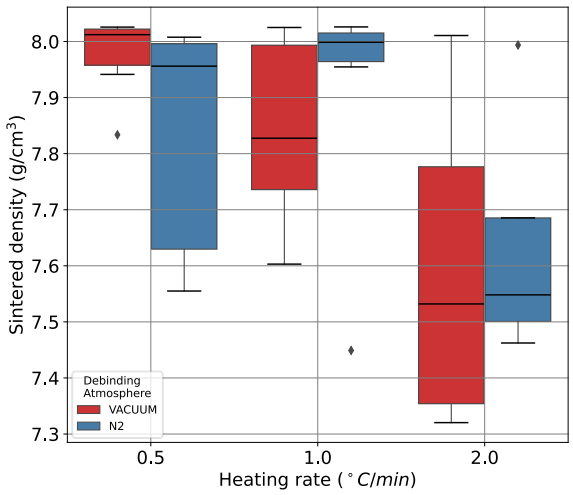

Figure 5. Sintered density of printed samples.
Source: Authors.

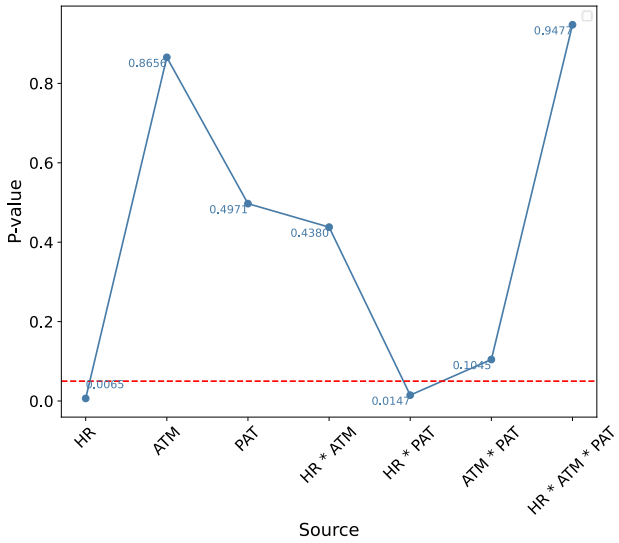

Figure 6. Three-way ANOVA of sintered density.
Source: Authors.

3.2 Thermal debinding and Sintering

Once the green samples were solvent debinded and considering the behavior of the composite material at TGA, ten TRS samples were thermally debinded for each heating rate (0.5 °C/min, 1 °C/min, and 2 °C/min) and finally sintered by the mechanism of SLPS (Super solidus Liquid Phase Sintering) [16,28,31].

After sintering, the density of the samples was measured. Density is a critical indicator of the final product's mechanical properties and overall quality. The accompanying box-and-whisker plot (Fig. 5) depicts the sintered density across different heating rates during the debinding process, under two distinct atmospheres: nitrogen (N2) and vacuum.

With the aim to identify how the parameters of the process interact in the final density a multilevel ANOVA was made, considering the parameters: HR: Heating rate, ATM: Thermal debinding atmosphere, PAT: Infill Pattern.

The three-way ANOVA analysis shown in Fig. 6, indicates that the heating rate holds a statistically significant influence on the sintered density with a p-value of 0.03276, which highlights its role as a critical parameter in the sintering process. The plot reveals that samples processed at a 0.5 °C/min heating rate generally exhibit a higher density, regardless of the atmosphere. The data suggest that slower heating rates facilitate a more effective release of the polymer decomposition gases, which may result in fewer defects during the sintering process. This is because, at higher heating rates, the rapid expansion of gases from the polymers could create flaws in the final pieces. Such control over the heating rate is crucial, as it can significantly enhance the integrity of the sintered parts by reducing porosity and cracks that compromise the material's mechanical properties.

Conversely, the sintered density does not appear to be significantly affected by either the nitrogen atmosphere or the vacuum environment, as their results overlap substantially at each heating rate.

Whereas the fill pattern was a significant factor in the green density of the parts, it does not seem to exert a considerable influence on the sintered density. This observation may occur since any initial differences in green density are mitigated or overshadowed by the dominant effects of the heating rate during sintering. This emphasizes the importance of optimizing the heating rate in the debinding process to achieve the desired material properties in the final sintered product.

To complement the analysis of sintered density, porosity measurements were conducted using image analysis on the cross-sectional area of the specimens, quantifying the pore area relative to the total area of the sample. The attached results illustrate these findings. According to ANOVA analysis with a p-value of 0.0057, the heating rate during debinding significantly affects porosity, with slower heating rates yielding lower porosity.

This correlation is depicted in the boxplot (Fig. 7), where it is evident that specimens subjected to slower heating rates exhibit significantly reduced porosity. This observation aligns with the previous discussion: slower heating rates allow the gases from the polymer decomposition to escape more gradually, diminishing the likelihood of pore formation which can occur due to rapid gas expansion at higher heating rates. This reinforces the conclusion that careful control of the heating rate is crucial for minimizing defects and ensuring the structural integrity of the sintered parts. Samples with lower porosity are better for withstanding internal pressures during thermal debinding, which is influenced by heating rates. This explains the results shown in Fig. 5 and the interaction between HR*PAT in Fig. 6.

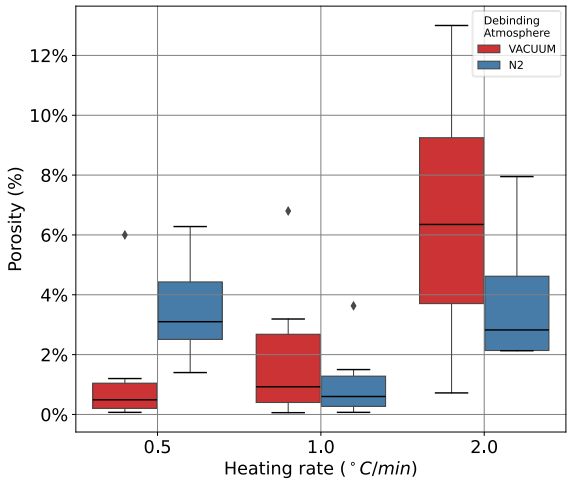

Figure 7. Final porosity.
Source: Authors.

3.2 Microstructure

A cross-sectional analysis of the sintered samples was conducted to identify the final microstructure. The samples did not exhibit differences between them, despite variations in parameters such as the printed pattern, heating rate, and debinding atmosphere. All the samples analyzed revealed a martensitic matrix surrounded by carbides, positioned intergranularly and at the grain boundaries, forming an intergranular network, as shown in Fig. 8. The formation of martensite occurred despite the cooling taking place in the furnace, rather than through rapid quenching. This is due to the high alloy content of M2 steel, which significantly increases its hardenability, allowing the transformation of austenite to martensite at the slower cooling rates typical of furnace cooling. Regarding the carbides, they are predominantly secondary carbides that precipitated during the cooling stage, influenced by the steel's chemical composition. The microstructure of the material remains unaffected by the process parameters because the SLPS mechanism is governed primarily by the temperature and the chemical composition of the steel [31].

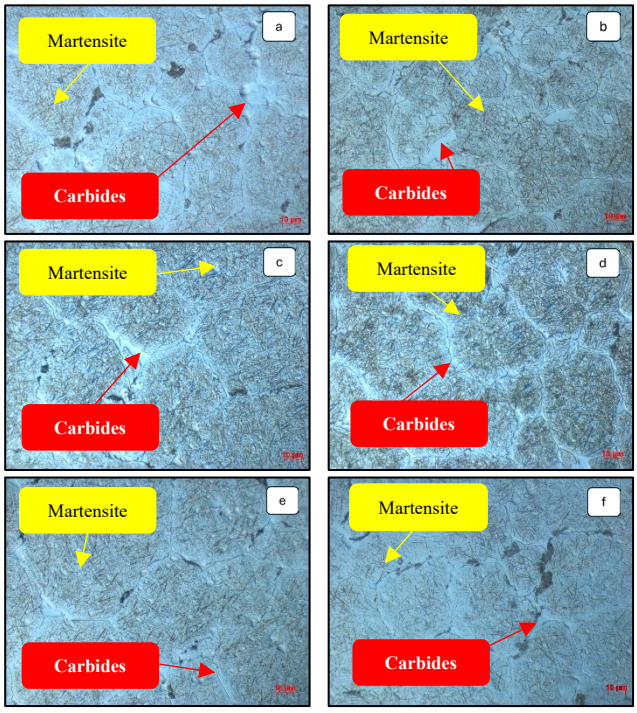

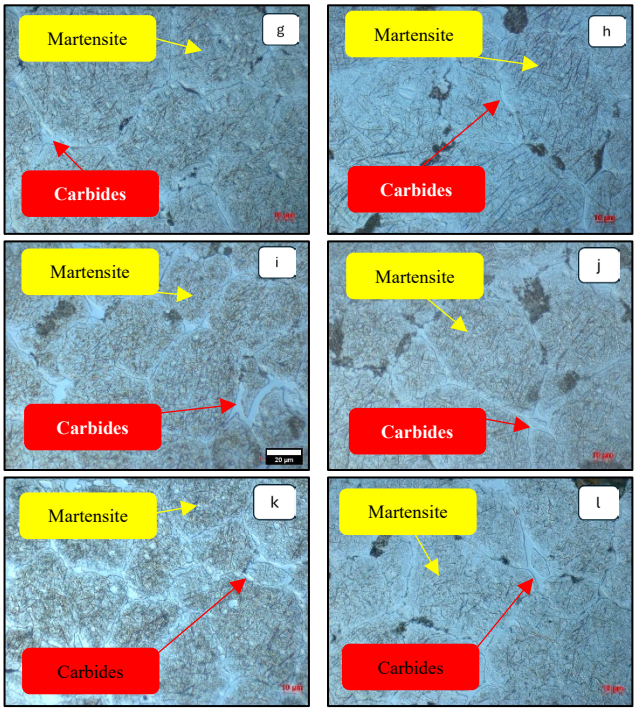

Figure 8. Metallography sections of printed and sintered samples. (a,c,e,g,i,k) Concetric patterns sintered at N2-0.5°C/min (a), N2-1°C/min (c), N2-2°C/min (e), Vacuum-0.5°C/min (g), Vacuum-1°C/min (i), Vacuum-2°C/min (k). (b,d,f,h,j,l) Linear pattern sintered at N2-0.5°C/min (b), N2-1°C/min (d), N2-2°C/min (f), Vacuum-0.5°C/min (h), Vacuum-1°C/min (j), Vacuum-2°C/min (l).
Source: Authors.

3.3 Mechanical properties

To evaluate the mechanical properties of the sintered materials, microhardness measurements were conducted at two positions on the samples: the edge and the center. These positions were chosen to assess the homogeneity achieved during the sintering process using the SLPS mechanism. The results, shown in Fig. 9, indicate a mean value of 727 HV for the linear strategy and 703 HV for the concentric strategy at the edge, while at the center, the values were 628 HV and 634 HV, respectively. However, some measurements deviated significantly from the mean, likely due to samples with higher porosity.

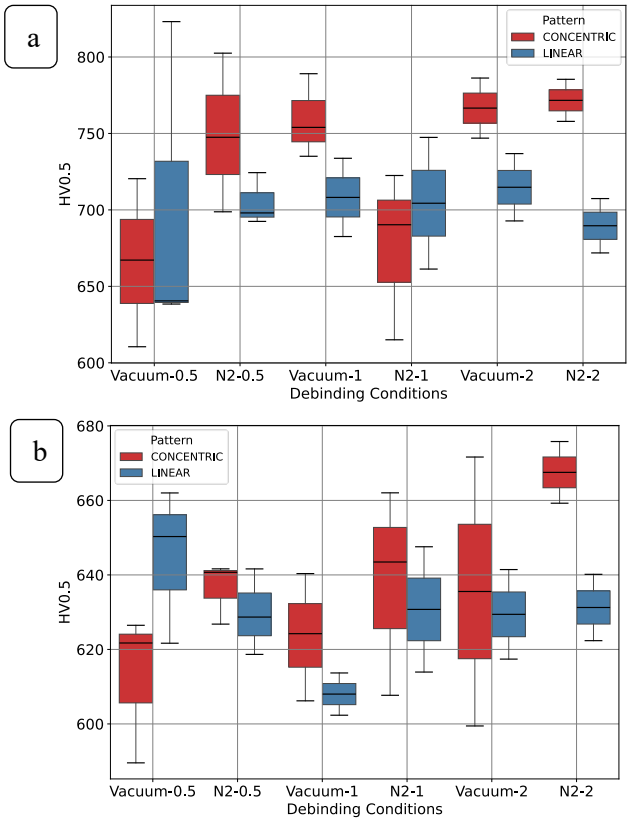

Figure 9. Microhardness of the sintered samples.
(a) Edge zone. (b) Center zone.
Source: Authors.

A three-way ANOVA confirmed these hardness observations, showing that the obtained values are not significantly influenced by parameters such as the printed pattern, heating rate, debinding atmosphere, or their interactions, as evidenced by the p-values in Fig. 10.

The TRS test results are presented in Figure 11. Samples subjected to thermal debinding in a nitrogen atmosphere exhibited the highest strength compared to those debinded in a vacuum atmosphere. This behavior correlates with the previously observed density (Fig. 1) and porosity (Fig. 7). Samples debinded in nitrogen retain more carbonaceous residues (from polymers), leading to a higher carbon content in the material. This increased carbon content enhances the formation of a liquid phase at high temperatures, promoting better densification, reduced porosity, and improved mechanical strength.

In contrast, samples debinded in a vacuum atmosphere may be exposed to oxygen, which can lead to oxide formation during thermal debinding. In such cases, the carbon residues from backbone degradation act as reducing agents for oxides in the initial stages of sintering, reducing the overall carbon content in the vacuum-debound samples [32], as shown in the carbon content measurements in Fig. 12. This reduction in carbon content significantly affects densification. Furthermore, the porosity introduced by high heating rates exacerbates this effect, resulting in lower mechanical strength.

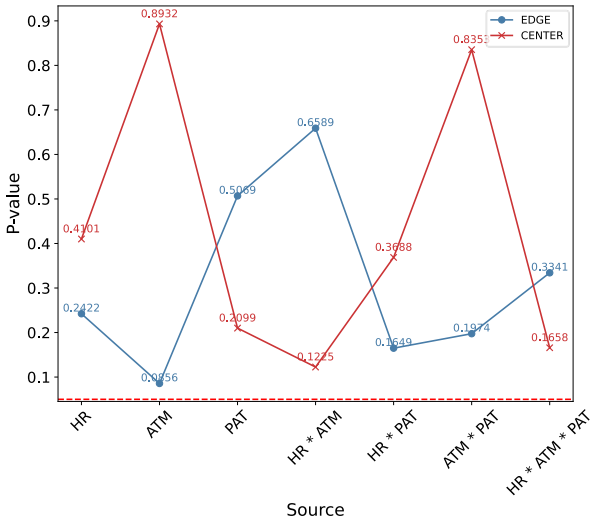

Figure 10. Three-way ANOVA of microhardness.
Source: Authors.

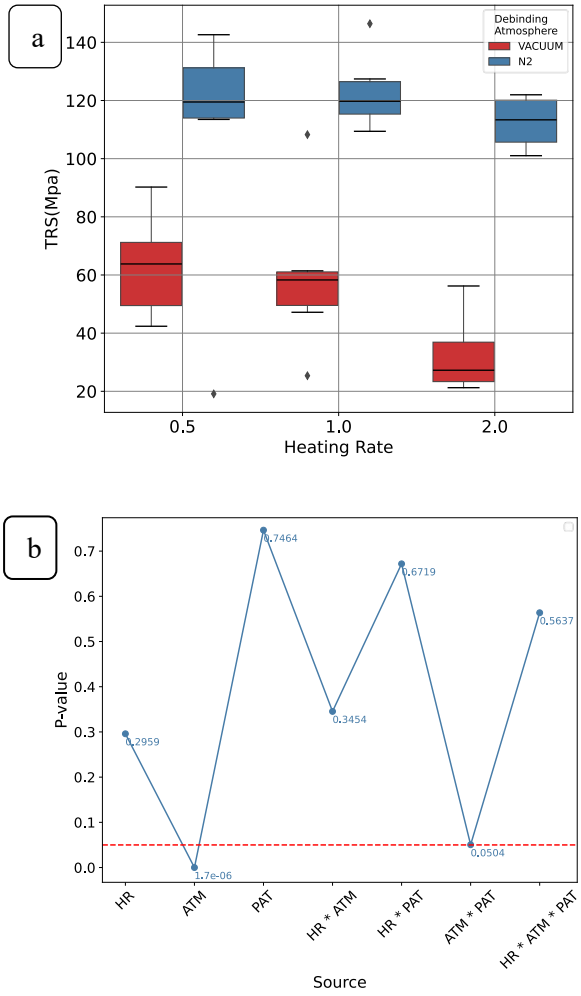

Figure 11. TRS results.
(a) Mechanical strength. (b)Three-way ANOVA of TRS.
Source: Authors.

Optical Emission Spectrometry confirms the final percentage of carbon: 1.33% in the nitrogen atmosphere and 1.27% in the vacuum atmosphere (Fig. 12). Based on the ANOVA results (Fig. 11b), it is demonstrated that the thermal debinding atmosphere significantly impacts the mechanical strength of the samples. This effect is compounded by the previously discussed printing strategy, which produces a greater presence of pores.

It is important to mention that the final material has a higher carbon content percentage than the initial material. Therefore, using active agents like hydrogen in thermal debinding could enhance the reduction of the residual carbonaceous products.

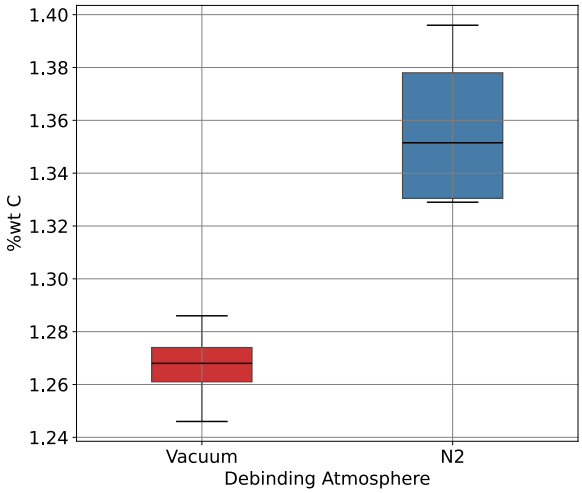

Figure 12. Final carbon weight percentage of the sintered samples.
Source: Authors.

Optical observations of the TRS samples reveal the presence of defects that persist after the debinding process (indicated by yellow arrows), demonstrating that the partial formation of liquid is insufficient to address these defects (Fig. 13).

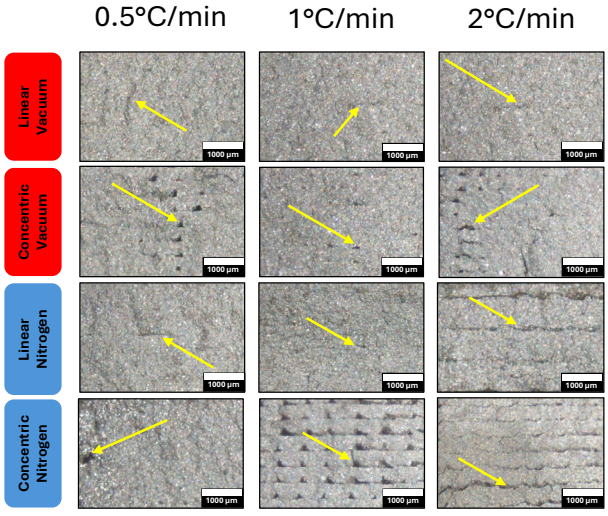

Figure 13. Optical micrographs of the transversal fracture of TRS samples.
Source: Authors.

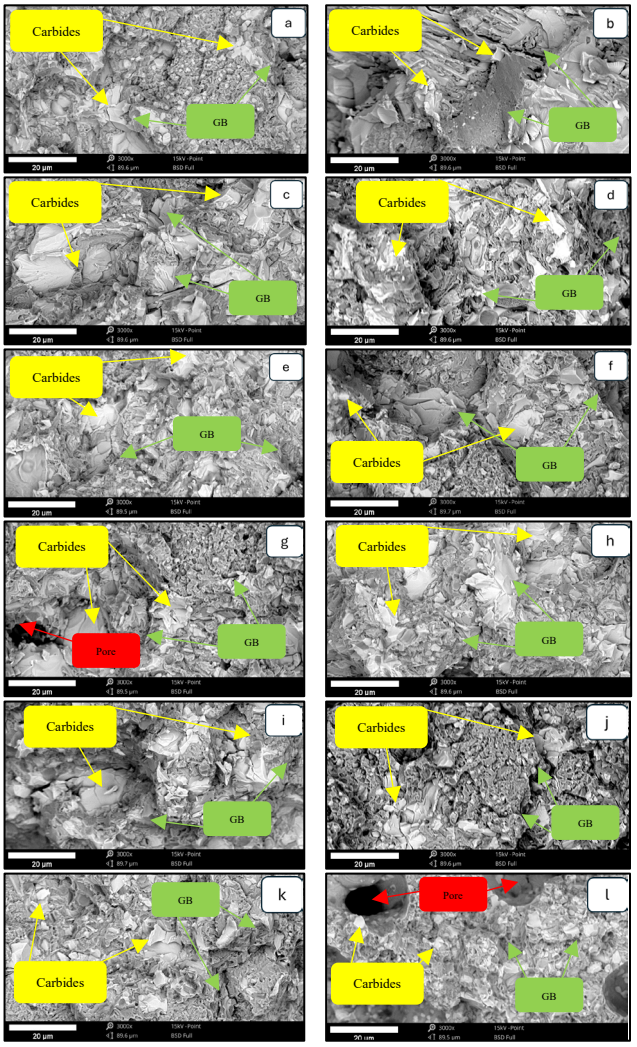

Figure 14. SEM micrographs of the transversal fracture of TRS samples. (a,c,e,g,i,k) Concetric patterns sintered at N2-0.5°C/min (a), N2-1°C/min (c), N2-2°C/min (e), Vacuum-0.5°C/min (g), Vacuum-1°C/min (i), Vacuum-2°C/min (k). (b,d,f,h,j,l) Linear pattern sintered at N2-0.5°C/min (b), N2-1°C/min (d), N2-2°C/min (f), Vacuum-0.5°C/min (h), Vacuum-1°C/min (j), Vacuum-2°C/min (l).
Source: Authors.

SEM micrographs (Fig. 14) of the fracture surfaces of TRS samples reveal the failure mode and mechanism, indicating predominantly brittle behavior in all cases. The brittle fracture is characterized by intergranular boundaries, where carbides precipitate during the sintering process, as shown in Fig. 8. These carbides are present both at the grain boundaries (GB) and intergranular, with some exhibiting cleavage. In the martensitic matrix, fractures exhibit a mixed mode of dimples and cleavage. However, the fracture surfaces observed by SEM are insufficient to explain the mechanical behavior of TRS, except when considering the influence of porosity.

4 Conclusions

Two different printing strategies were studied using a composite material for the FFF process, providing a foundation for future research to determine the optimal

parameters for producing functional parts. The main findings of this study are as follows:

Concentric strategies tended to result in more defects, which persisted through the SLPS process.

Higher heating rates during thermal debinding promoted defects due to internal pressure caused by the decomposition of polymeric products.

The findings indicate that the thermal debinding atmosphere has a significant impact on the final carbon content and, consequently, on the mechanical properties of the material. It is suggested to investigate the use of active atmospheres rich in hydrogen (H_2) during debinding and sintering. These atmospheres could facilitate the removal of carbonaceous residues and allow for more precise control of the carbon content, improving densification and reducing porosity in the sintered parts.

Based on the results obtained, it is possible to produce tools such as hot punching tools through the Fused Filament Fabrication (FFF) technique. This advancement allows us to perform real tests to evaluate the performance of these tools under high-temperature and wear conditions.

Acknowledgements

The authors thank the Powder Metallurgy Laboratory of "Universidad Nacional de Colombia, Sede Bogota" and the "Centro de Materiales y Ensayos of SENA, Regional Distrito Capital SGPS-12351-2024 and SGSPS-13030-2024" for the logistical, technical, human, and financial support of the project. The project funded this research, "Technological development for the manufacture of metal tools using additive manufacturing techniques based on extrusion for high temperature and wear applications used by the Colombian auto parts industry" with the code 82305 - 110189082305 and contingent recovery financing contract number 2021-1012 of 2021 celebrated between the Colombian institute of educational credit and technical studies abroad, "Mariano Ospina Pérez"—ICETEX, the Ministry of Science, Technology and Innovation, and the National University of Colombia.

References

[1] Zhou, L., et al., Additive manufacturing: a comprehensive review sensor. Multidisciplinary Digital Publishing Institute (MDPI), 24(9), art. 2668, 2024. DOI: https://doi.org/10.3390/s24092668

[2] Imran, M.M., Che-Idris, A., De-Silva, L.C., Kim, Y.B., and Abas, P.E., Advancements in 3D printing: directed energy deposition techniques, defect analysis, and quality monitoring. Technologies (Basel), 12(6), art. 0086, 2024. DOI: https://doi.org/10.3390/technologies12060086

[3] Shah, A., Aliyev, R., Zeidler, H., and Krinke, S., A review of the recent developments and challenges in wire arc additive manufacturing (WAAM) process. Journal of Manufacturing and Materials Processing, 7(3), art. 0097, 2023. DOI: https://doi.org/10.3390/jmmp7030097

[4] Ghanadi, N., and Pasebani, S., A review on wire-laser directed energy deposition: parameter control, process stability, and future research paths. Journal of Manufacturing and Materials Processing, Multidisciplinary Digital Publishing Institute (MDPI), 8(2), art. 0084, 2024. DOI: https://doi.org/10.3390/jmmp8020084

[5] Gong, X., Anderson, T., and Chou, K., Review on powder-based electron beam additive manufacturing technology. Manufacturing Review, EDP Sciences, (1), art. 4001, 2014. DOI: https://doi.org/10.1051/mfreview/2014001

[6] Li, Z., et al., High deposition rate powder-and wire-based laser directed energy deposition of metallic materials: a review. International Journal of Machine Tools and Manufacture, (181), art. 103942, 2022. DOI: https://doi.org/10.1016/j.ijmachtools.2022.103942

[7] Jorge, V.L., Teixeira, F.R., Wessman, S., Scotti, A., and Henke, S.L., The impact of multiple thermal cycles using CMT® on microstructure evolution in WAAM of Thin walls made of AlMg5. Metals (Basel), 14(6), art. 0717, 2024. DOI: https://doi.org/10.3390/met14060717

[8] Heo, S., Lim, Y., Kwak, N., Jeon, C., Choi, M., and Jo, I., Impact of heat treatment and building direction on tensile properties and fracture mechanism of Inconel 718 produced by SLM process. Metals (Basel), 14(4), art. 0440, 2024. DOI: https://doi.org/10.3390/met14040440

[9] Honu, E., Emanet, S., Chen, Y., Zeng, C., and Mensah, P., Effects of low-temperature heat treatment on mechanical and thermophysical properties of Cu-10Sn alloys fabricated by laser powder bed fusion. Materials, 17(12), art. 2943, 2024. DOI: https://doi.org/10.3390/ma17122943

[10] Banerjee, S., and Joens, C.J., Debinding and sintering of metal injection molding (MIM) components. Handbook of Metal Injection Molding, pp. 133–180, 2012. DOI: https://doi.org/10.1533/9780857096234.1.133

[11] Kukla, C., Duretek, I., Schuschnigg, S., Gonzalez-Gutierrez, J., and Holzer, C., Properties for PIM feedstocks used in fused filament fabrication. World PM 2016 Congress and Exhibition, 2016.

[12] Kukla, C., Gonzalez-Gutierrez, J., Cano, S., and Hampel, S., Fused filament fabrication (FFF) of PIM feedstocks. Proceedings of VI Congreso Nacional de Pulvimetalurgia y I Congreso Iberoamericano de Pulvimetalurgia, 2017.

[13] Cano, S., et al., Additive manufacturing of Zirconia parts by fused filament fabrication and solvent debinding: selection of binder formulation. Additive Manufacturing, 26(11), pp. 117–128, 2019. DOI: https://doi.org/10.1016/j.addma.2019.01.001

[14] Tirado-González, J.G., Esguerra-Arce, J., Esguerra-Arce, A., and Herrera-Quintero, L.K., 3D printing Iron/Iron oxide composites by metal material extrusion from an industrial waste. JOM, 76(4), pp. 1924–1936, 2024. DOI: https://doi.org/10.1007/s11837-024-06371-2

[15] Gil-Plazas, A.F., Villamil Galindo, A.D., Rubiano Buitrago, J.D., Viloria Estrada, A., y Herrera-Quintero, L.K., La industria 4.0 en tu casa: impresión de prototipos de herramientas de punzonado para trabajo en caliente con impresoras de modelado por deposición fundida de bajo coste. Reto, pp. 23–35, 2021.

[16] Gil-Plazas, A.F., Rubiano-Buitrago, J.D., Boyacá-Mendivelso, L.A., and Herrera-Quintero, L.K., Solid-state and super solidus liquid phase sintering of 4340 Steel SLM powders shaped by fused filament fabrication. Revista Facultad de Ingeniería, 31(60), art. 13913, 2022. DOI: https://doi.org/10.19053/01211129.v31.n60.2022.13913

[17] Rubiano-Buitrago, J.D., Gil-Plazas, A.F., Boyacá-Mendivelso, L.A., and Herrera-Quintero, L.K., Fused filament fabrication of WC-10Co Hardmetals: a study on binder formulations and printing variables. Journal of Manufacturing and Materials Processing, 8(3), art. 30118, 2024 DOI: https://doi.org/10.3390/jmmp8030118

[18] Costa, J.M., Sequeiros, E.W., and Vieira, M.F., Fused filament fabrication for metallic materials: a brief review. Materials, Multidisciplinary Digital Publishing Institute (MDPI), 16(24), art. 7505, 2023. DOI: https://doi.org/10.3390/ma16247505

[19] Myers, N.S., and Heaney, D.F., Metal Injection Molding (MIM) of high-speed tool steels. Handbook of Metal Injection Molding, pp. 516–525, 2012. DOI: https://doi.org/10.1533/9780857096234.4.516

[20] Naranjo, J.A, Berges, C., Gallego, A., and Herranz, G., A novel printable high-speed steel filament: Towards the Solution for wear-resistant customized tools by AM alternative. Journal of Materials Research and Technology, 11(3), pp. 1534–1547, 2021. DOI: https://doi.org/10.1016/j.jmrt.2021.02.001

[21] Thompson, Y., Gonzalez-Gutierrez, J., Kukla, C., and Felfer, P., Fused filament fabrication, debinding and sintering as a low-cost additive manufacturing method of 316L stainless steel. Additive Manufacturing, 30(5), art. 100861, 2019. DOI: https://doi.org/10.1016/j.addma.2019.100861.

[22] Gonzalez-Gutierrez, J., Arbeiter, F., Schlauf, T., Kukla, C., and Holzer, C., Tensile properties of sintered 17-4PH stainless steel fabricated by material extrusion additive manufacturing. Materials letters, (248), pp. 165–168, 2019. DOI: https://doi.org/10.1016/j.matlet.2019.04.024

[23] Gonzalez-Gutierrez, J., Kukla, C., Schuschnigg, S., Duretek, I., and Holzer, C., Fused Filament Fabrication for Metallic Parts. 2016.
[24] Abel, J., et al., Fused Filament Fabrication (FFF) of metal-ceramic components. Journal of Visualized Experiments, 2019(143), pp. 1–13, 2019. DOI: https://doi.org/10.3791/57693
[25] Kukla, C., Gonzalez-Gutierrez, J., Burkhardt, C., Weber, O., and Holzer, C., The production of magnets by FFF-Fused Filament Fabrication. Proceedings Euro PM 2017: International Powder Metallurgy Congress and Exhibition, 2017.
[26] Gonzalez-Gutierrez, J., Godec, D., Kukla, C., Schlauf, T., Burkhardt, C., and Holzer, C., Shaping, debinding and sintering of steel components via fused filament fabrication. 16th International Scientific Conference on Production Engineering - CIM2017, 2017.
[27] Lengauer, W., et al., Fabrication and properties of extrusion-based 3D-printed hardmetal and cermet components. International Journal of Refractory Metals and Hard Materials, 82(2), pp. 141–149, 2019. DOI: https://doi.org/10.1016/j.ijrmhm.2019.04.011.
[28] German, R.M., Suri, P., and Park, S.J., Review: liquid phase sintering. Journal of Materials Science, 44(1), pp. 1–39, 2009. DOI: https://doi.org/10.1007/s10853-008-3008-0.
[29] German, R.M., Densification of prealloyed tool steel powders: sintering model. International Journal of Powder Metallurgy, pp. 49–61, 1986.
[30] German, R.M., Computer model for the sintering densification of injected molded M2 tool steel. International Journal of Powder Metallurgy, pp. 57–67, 1999.
[31] German, R.M., Liquid phase sintering. Ed. Tongfang CNKI Technology Co., Ltd. Beijing. China, 1985. DOI: https://doi.org/10.16309/j.cnki.issn.1007-1776.2003.03.004
[32] Herranz, G., Control of carbon content in metal injection molding (MIM). En: Handbook of Metal Injection Molding, Ed. Elsevier Inc., 2012, pp. 265–304. DOI: https://doi.org/10.1533/9780857096234.2.265.

T.A Amaya Villabón, is BSc. Eng in Mechanical Engineering from the Universidad Nacional de Colombia. He is currently working on additive manufacturing of ceramic materials to obtain a bachelor's degree in Mechatronics Engineering.
ORCID: 0009-0004-4871-8780.

A.F Gil Plazas, is a MSc.in Materials and Processes from the Universidad Nacional de Colombia and a BSc. Eng. in Mechanical Engineering from ECCI University. He is currently working on additive manufacturing using Wire Arc Additive Manufacturing (WAAM) at SENA and serves as the SENNOVA leader of the Materials and Testing Center.
ORCID: 0000-0001-6585-9121.

J.D Rubiano Buitrago, is a MSc. in Materials and Processes from the Universidad Nacional de Colombia, and a Mechanical Engineer from Universidad Distrital, Colombia. He is currently pursuing a PhD. in Materials and Science Engineering, focusing on additive manufacturing using Fused Filament Fabrication (FFF) in hard metals.
ORCID: 0000-0003-3491-8373.

L.K Herrera Quintero, is an Associate Professor in the Mechanical and Mechatronics programs at the School of Engineering, Universidad Nacional de Colombia. Holds a PhD. in Materials Science from Universidad de Sevilla, Spain, and has completed two postdoctoral positions in materials and advanced manufacturing technologies. Serves as the Academic Coordinator of the Doctorate Program in Science and Technology of Materials and Coordinator of the Laboratory University Division (UNALab). Strategic promoter of Digital Transformation at the National University of Colombia, he focuses on promoting capacities and empowering the community to tackle challenges related to a human-centered society, sustainability, and resilience. He works to reduce barriers to incorporating competitive ecosystems and generating solutions aligned with the university's mission goals.
ORCID: 0000-0003-2002-4336.